Title: Endogenous suspension and reset of consciousness: 7T fMRI brain mapping of the extended cessation meditative endpoint

Authors

Winson F.Z. Yang[1,2], [+]Akila Kadambi[3,4], [+]Kilian Abellaneda-Pérez[5,6], Grace Mackin[1,2,7], Isidora Beslic[1,2,7], Ruby Potash[1,2], Terje Sparby[8,9,10], Matthew D. Sacchet[1,2]* (meditationadministration@mgh.harvard.edu)

[+]Denotes co-second-authors

Affiliations

[1]Meditation Research Program, Department of Psychiatry, Massachusetts General Hospital, Harvard Medical School, Boston, USA

[2]Athinoula A. Martinos Center for Biomedical Imaging, Department of Radiology, Massachusetts General Hospital, Harvard Medical School, USA

[3]Dept. of Psychiatry and Biobehavioral Sciences, David Geffen School of Medicine, University of California, Los Angeles, USA

[4]Brain and Creativity Institute, Dornsife College of Letters, Arts, and Sciences, University of Southern California, Los Angeles, USA

[5]Institut Guttmann, Institut Universitari de Neurorehabilitació adscrit a la Universitat Autònoma de Barcelona, Badalona, Spain

[6]Department of Medicine, Faculty of Medicine and Health Sciences, Institute of Neurosciences, University of Barcelona, Barcelona, Spain

[7]Northeastern University, Boston, USA

[8]Steiner University College, 0260 Oslo, Norway

[9]Department of Psychology and Psychotherapy, Witten/Herdecke University, 58455 Witten, Germany

[10]Integrated Curriculum for Anthroposophic Psychology, Witten/Herdecke University, 58455 Witten, Germany

Abstract

Extended cessation (EC), an advanced meditative state in which consciousness is volitionally suspended and later reset with immense mental clarity, equanimity, and peace, offers an endogenous model for investigating the mechanisms of consciousness. Using ultra-high-resolution 7T fMRI with dense within-subject sampling (N=3), we quantified whole-brain activity, functional and effective connectivity, cortical gradients, and eigenmodes, and related them to chemoarchitecture and cognitive maps. EC is marked by increased activity in unimodal regions, down-regulation in transmodal regions, subcortex, and brainstem, an expansion of the principal gradient, and decrease in low-order global eigenmodes. Cognitive decoding linked EC to heightened perceptual clarity and attention, least with mental suffering, and co-varied with histaminergic H_3 receptors topology. These findings challenge predictions of Global Neuronal Workspace and Integrated Information Theory, while supporting the Active Inference Framework. More broadly, EC demonstrates that consciousness can cease without global suppression, suggesting a potential "reset" mechanism that fosters equanimity and the potential for flourishing.

Keywords: advanced meditation, extended cessation, consciousness, subcortical, brainstem, functional connectivity, chemoarchitecture

Introduction

In most scientific and clinical frameworks, wakefulness is assumed to entail ongoing subjective consciousness[1]. Advanced meditative states challenge this assumption by showing that consciousness can be radically thinned to minimal 'content-free' awareness[2,3] or even entirely suspended momentarily[4-7] or for an extended duration[8]. These findings highlight the extraordinary plasticity of consciousness, raising fundamental questions for theories of consciousness, including Global Neuronal Workspace, Integrated Information Theory, and Active Inferences Framework, and their relevance to human flourishing[9,10].

Advanced meditation situates these rare states within a broader scientific agenda: understanding consciousness as a trainable and reconfigurable capacity across meditative development[11,12]. This systematic mental training can lead to meditative endpoints, variously described as "awakening"[13,14], "beatitude"[15], "salvation"[16], or "enlightenment"[13,14], that entail profound shifts in perception, emotion, and self-processing. Studying such endpoints offers not only a natural experiment for testing theories of consciousness but also insights into how such they can induce a "reset" of consciousness that fosters equanimity, resilience, and well-being, all of which are critical priorities in global mental health[17-19].

Here, we study extended cessation (EC), a rare meditative endpoint where practitioners report temporary suspensions of ordinary consciousness and mental activities[4,8]. EC can vary from minutes to days, is entered and exited volitionally, and is frequently followed by profound psychological aftereffects, including extreme sense of relief, clarity, openness, peace, equanimity, heightened sensory sensitivity, significant reduction in mental suffering, reduced repetitive thoughts, stoppage of negative self-talk, and an absence of inner narration[8,18,19]. Unlike non-conscious states induced by pharmacological agents (e.g., anesthesia or psychedelics)[20,21], EC is unique in being endogenous, reversible, precisely timed, and followed by heightened well-being, making it an excellent natural experiment for probing the mechanisms of consciousness. One canonical form of EC found in Theravada Buddhism is Nirodha Samāpatti[8,22-24]. Here, we investigate the broader neurobiological principles of EC without making definitive claims about its doctrinal interpretation[4,6,7]. Please refer to Laukkonen et al. for a recent discussion of the historical and theoretical context of Nirodha Samāpatti[8]. It is noteworthy that Nirodha Samāpatti

is considered to be among the highest, or the highest, meditative attainment in some interpretations of Theravada Buddhism[25,26].

From a neuroscience perspective, studying EC offers a powerful opportunity to explore the fundamental nature and mechanisms of consciousness. A central limitation in current consciousness research is the absence of an endogenous and reversible method to suspend awareness while preserving physiological stability[20,21] and enabling prospectively timed re-emergence[8,23]. EC addresses this gap[7,8]. Compared to sleep, anesthesia, and disorders of consciousness, EC constitutes a fourth experimental context in its uniqueness self-initiate and control consciousness. This enables precise examination of transition dynamics at entry and exit and the mechanisms that dismantle and reinstate conscious access. Additionally, the notable aftereffects of EC described above may relate to significant neuroplasticity and reorganization of the brain, potentially informing techniques to enhance cognitive function, emotional regulation, overall wellbeing and happiness, and thriving.

Current competing frameworks of consciousness make testable predictions for EC. Global Neuronal Workspace (GNW) predicts a collapse of long-range connectivity and reduced feedback connectivity during suspension of consciousness[27] while Integrated Information Theory (IIT) predicts a decrease in network differentiation during non-conscious states[28]. In contrast, the Active Inference Framework (AIF) predicts down-weighting of sensory precision via thalamo-cortical gating during non-conscious states[29]. The distinct features of EC allow comparison among theories about how consciousness is represented and suspended in the human brain.

Here we present the first neuroscientific, empirical investigation of EC, using ultra-high-resolution 7T functional magnetic resonance imaging (fMRI) to investigate the whole-brain activity, connectivity, and causal dynamics of network organization during EC. The ultra-high spatial resolution of 7T imaging allows for precise measurement of small but critical brain structures that are central to consciousness and arousal regulation, such as the thalamus, brainstem, and subcortical nuclei. This methodology is particularly powerful for the study of consciousness, where transitions between conscious and non-conscious brain states may be mediated by subtle shifts in deep-brain activity. Moreover, we used a novel and systematic neurophenomenological

approach to rigorously examine the subjective experience of EC, enabling a rare convergence of first-person insight and third-person measurement.

This study provides important initial evidence for the neuroscience of EC and related fundamental aspects of consciousness, with potential therapeutic implications for human flourishing. In this study we sought to answer three key questions: (1) What brain reconfiguration accompanies voluntary suspension of consciousness?; (2) What are the causal brain dynamics of EC; and (3) Which neurochemical systems are implicated, as inferred from spatial coupling to normative receptor distributions?

Our findings indicate that consciousness can be suspended without global cortical suppression. During EC, unimodal systems (e.g., visual and dorsal-attention networks) remain selectively engaged while transmodal hubs and thalamo-striatal circuits are down-regulated; the principal cortical gradient polarizes rather than flattens; and network–neurochemical coupling aligns with histaminergic (H_3) precision control of sensory gating. Meta-analytic decoding demonstrated that EC is functionally aligned with perception and attention, while being least associated with mental suffering and distress. This neuronal signature is most consistent with AIF, constrains GNW theory, and challenges IIT. This study demonstrates that the human brain can volitionally dismantle and reassemble conscious processing, offers a radical model for testing theories of consciousness, and highlights the possibility that consciousness can 'reset' and orient toward equanimity and flourishing.

Results

EC Phenomenology

Detailed demographic of participants (N = 3) are provided in Methods. Participant endorsement of EC phenomenology is presented in **Fig. 1**. Here, we summarize the key phenomenology for the setup, entry, exit, and afterglow of EC.

Setup. Participants typically used advanced absorption concentration meditation (ACAM) to set up EC. ACAM is a series of meditative absorption states accompanied by blissful sensations, emotional happiness, and equanimity, followed by an increasing reduction of input from the physical environment and the reduction of contents of consciousness to a bare minimum

experience. One participant who had previously trained using ACAM for setup, no longer necessarily needed ACAM to enter EC. Additionally, all but one participant incorporated elements of advanced investigative insight meditation (AIIM), that is, a neutral observation of phenomena, as part of their preparatory routine for EC.

Onset. All participants reported that internal verbalization (thinking), body sensations, and feeling ceased during the onset of EC. With one exception, participants reported no primary experiential emphasis on either incongruence, transient nature of experience, or self-lessness (these are typically present during momentary cessations).

EC. During EC, participants reported that typically all consciousness experience was completely offline.

Exit. Upon emerging from EC, all participates reported that biographical memory and ego-centered cognitive processing were typically absent, and they did not perceive any separation between themselves and the environment. All participants reported a vivid clarity of mind and an experience of objectless awareness. All but one participant reported the return of mental activity in a specific sequence: first thought, then bodily sensation, and finally internal verbalization.

Afterglow. After EC, all participants reported typically experiencing intense sensory vividness, accompanied by a strong and lasting peace. They all also reported typically being inclined to solitude, and many described a deep, abiding joy.

Brain activity during EC: Regional homogeneity (ReHo)

Comprehensive results/summary tables of significant regions are included in the **Supplementary excel file**. Results are visualized in **Fig. 2**. Here, we only provide a summary of the results.

Across both counting and memory control conditions. In the cortex, EC, compared to both counting and memory conditions, was associated with higher ReHo values in the bilateral visual and posterior cortices, frontal eye fields, temporal poles, left prefrontal, parietal, temporal cortices, and right dorsomedial prefrontal cortex; and lower ReHo values in the bilateral prefrontal,

159 somatomotor, temporal, and orbitofrontal cortices, posterior frontal opercula and insula, left
160 precuneus-posterior cingulate cortex, and right cingulate cortex.

161 In the subcortex, EC was primarily associated with decreased ReHo values. Regions
162 include the ventoposterior (THA-VP) and right dorsoanterior (THA-DA) thalamus, left anterior
163 putamen, right hippocampus, medial amygdala, anterior caudate, and globus pallidus. Increased
164 ReHo was also seen in the left hippocampus, medial amygdala, and shell of the nucleus accumbens.

165 In the brainstem, EC was associated with higher ReHo values in the median raphe, raphe
166 obscurus, left inferior medullary reticular formation (MRt), mesencephalic reticular formation,
167 inferior olivary nucleus, viscero-sensory-motor nuclei complex, right alpha part of the
168 parvicellular reticular nucleus, superior MRt, and superior olivary complex. EC was also
169 associated with lower ReHo values in the dorsal raphe, left locus coeruleus, subcoeruleus,
170 laterodorsal tegmental nucleus-central gray of the rhomboencephalon, right cuneiform nucleus,
171 superior colliculus, and parabrachial pigmented nucleus complexes of the ventral tegmental area
172 (VTA-PBP).

173 In the cerebellum, EC was associated with higher ReHo values in cerebellum regions 6
174 (divided attention) and 10 (autobiographical recall and interference resolution).

175 Additional significant regions of interest (ROIs) for each control condition are presented
176 below.

177 ***EC vs counting control condition.*** Additionally, EC, compared to the counting control
178 condition, was associated with lower ReHo values in the left dorsoposterior thalamus (THA-DP),
179 raphe magnus, left substantia nigra, and red nucleus.

180 ***EC vs memory control condition.*** In the subcortex, EC compared to the memory control
181 condition, was associated with higher ReHo values in the left posterior globus pallidus and
182 putamen, and right nucleus accumbens. Decreased ReHo values were found in the bilateral lateral
183 amygdala and right ventroanterior (THA-VA) thalamus and THA-VP. In the brainstem, higher
184 ReHo values were found in the left isthmic reticular formation, pedunculotegmental nucleus,
185 superior MRt, and right medial parabrachial nucleus; and lower ReHo values in the right inferior
186 olivary nucleus and microcellular tegmental nucleus – prabigeminal nucleus. In the cerebellum,

EC, compared to the memory control condition, was associated with lower ReHo in the cerebellar region 4 (associated with action observation).

Full correlations for the 123 cognitive terms are reported in the **Supplementary excel file**.

Functional connectivity: Network-based statistics (NBS)

Comprehensive results/summary tables of significant regions are included in the **Supplementary excel file** and results are visualized in **Fig. 3a, b**. Here, we only provide a summary of the results.

Across both counting and memory control conditions. Notable findings include widespread lower functional connectivity throughout the brain, mostly between the brainstem and cortical networks, including the default-mode network (DMN), and between cortical networks, such as DMN-control network [CN], and CN-salience network (SN) during EC compared to both counting and memory control conditions.

EC vs counting control condition. We observed reduced connectivity between the brainstem and somatomotor (SMN) and dorsal attention (DAN) networks (**Fig. 3a**) during EC compared to the counting condition.

EC vs memory control condition. Interestingly, during EC, reduced functional connectivity between cortical networks such as the DAN, limbic network (LN), VN, and brainstem were notable (**Fig. 3b**). Additional reduced connectivity were found between the cerebellum and left subcortex.

Effective connectivity: Directed network-based statistics (dNBS)

Results, including excitatory and inhibitory connections, and averaged weighted in-degree and out-degree are visualized in **Fig. 3c, d**. Here, we only provide a summary of the results.

Across both counting and memory control conditions. No similar excitatory or inhibitory connections were found across both control conditions compared to EC.

EC vs counting control condition. No notable excitatory or inhibitory connections were found between EC and the counting control condition (**Fig. 3c**).

EC vs memory control condition. Both excitatory and inhibitory connections were observed (**Fig. 3d**) during EC compared to the memory condition. Interestingly, inhibitory connections extend to nearly all brain networks, including the subcortex and brainstem. Specifically, we observed primarily excitatory connections to and from the left VN and brainstem, and inhibitory connections to and from the bilateral SMN, left SN, right CN and VN.

Brain reorganization: Connectivity gradients

Description and distribution of gradient values. The principal gradient depicted in the study aligns with previous research[30-34], which identified a potentially hierarchical axis of functional connectivity similarity variance. This axis extends from unimodal regions, primarily located in the somatomotor cortex, to transmodal regions centered around the DMN and LN (**Fig. 4a**). Lower principal gradient values reflect greater functional connectivity similarity to unimodal cortex, whereas higher principal gradient values reflect greater functional connectivity similarity to transmodal cortex. We observed a wider range of gradient distribution across all networks. (**Fig. 4b)**. Moreover, EC demonstrated an expansion of principal gradients compared to the two control conditions (**Fig. 4c**). Results for the bootstrapped t-tests at the ROI-level are presented in **Fig. 4d**, at the network-level **in Fig. 4e**. Significant results are also presented in the **Supplementary excel file**. Below, we summarize the results.

Across both counting and memory control conditions. LMM at the network-level revealed that EC exhibited greater gradient values in the CN. At the ROI-level, EC demonstrated greater gradient values in the right frontal operculum insula, parietal cortex, and lateral PFC; and lower gradient values in the bilateral visual cortex within the visual network (VN). No additional significant gradient values were found.

Cortical dynamics: Geometric eigenmodes

Across both counting and memory control conditions. LMM revealed no significant differences between EC and either counting or memory control conditions for mean, max, and total power or energy in any eigengroups. However, LMM revealed significant differences in main

239 effects of task conditions between EC and control conditions for mean, max, or total power or
240 energy (**Fig. 5**). Specifically, EC, compared to the counting condition, had lower max ($b = -0.09$,
241 $p = 0.006$) and total ($b = -0.14$, $p < 0.001$) power. Additionally, compared to the memory control
242 condition, EC has lower mean ($b = -0.15$, $p < 0.001$), max ($b = -0.31$, $p = 0.009$), and total ($b = -$
243 0.16, $p < 0.001$) energy, and lower mean ($b = -0.32$, $p = 0.007$), max ($b = -0.21$, $p < 0.001$), and
244 total ($b = -0.37$, $p = 0.001$) power.

245 ***Neurotransmitter systems receptor density: Partial least squares correlation (PLSC)***

246 PLSC extracted one significant latent variable relating neurotransmitter systems receptor
247 densities to delta-weighted-degree maps, explaining 98.85% of the covariance between the two
248 datasets ($p_{spin} = 0.023$, one-tailed). Additionally, a positive correlation was found between the
249 latent variables ($r = 0.42$, $p < 0.001$, **Fig. 6a**). We also computed the loadings for each receptor
250 (**Fig. 6b**) and delta-weighted-degree map (**Fig. 6c**), where positively loaded receptors co-vary with
251 positively loaded delta-weighted-degree in positively scored brain regions and similarly for
252 negative loadings[35]. Projecting the neurotransmitter systems receptor density patterns back onto
253 the delta-weighted-degree weights reflects how well a brain area exhibits the receptor and delta-
254 weighted-degree weighted pattern, referred to here as 'receptor scores' and 'delta-weighted-degree
255 scores', respectively (**Fig. 6d, e**).

256 Metabotropic glutamate receptor 5 ($mGluR_5$), serotonin $5HT_4$, and dopamine D_1 displayed
257 the greatest positive loadings while histamine H_3 displayed the only negative loading (**Fig. 6b**).
258 Non-significant loadings include serotonin transporter 5HTT, mu-opioid receptor MOR,
259 norepinephrine transporter NET, and $GABA_A$. Both EC-Counting and EC-Memory delta
260 weighted-degree maps have similar negative loadings (**Fig. 6c**). This suggests that the combination
261 of H_3 receptor distributions co-vary with EC-related weighted-degree values in unimodal regions
262 (**Fig. 6d**). EC reduces connectivity where $mGluR_5/5HT_4/D_1$ receptors are abundant and increases
263 connectivity where H_3 receptors are abundant, relative to both control tasks. Examining the brain
264 scores, transmodal regions (PFC, PCC, temporal areas), where $mGluR_5/5HT_4/D_1$/NMDA receptors
265 are rich, decrease connectivity during EC relative to both controls (**Fig. 6e**). In contrast, primary
266 sensory and motor cortices where H_3 receptors are plenty, increase connectivity during EC.

Collectively, these results demonstrate a direct link between whole-brain molecular receptor distributions and EC.

Neurosynth data-driven cognitive terms decoding analysis

Across both counting and memory control conditions. Correlation analysis revealed that EC was positively associated with action, attention, fixation, gaze, planning, spatial attention, visual attention, and visual perception. These terms are associated with perception and planning. In contrast, negative associations were found with terms such as anxiety, arousal, eating, emotion, fear, loss, mood, pain, stress, and valence. These terms are associated with mental suffering and psychological distress. Results are visualized in **Fig. 2**.

EC vs counting control condition. EC was additionally positively associated with imagery and object recognition.

EC vs memory control condition. EC was additionally positively associated with selective attention and efficiency.

Discussion

Using ultra-high-resolution 7T functional MRI, we present the first neural characterization of an extraordinary non-conscious state of extended cessation (EC). We used an intensive within-subject, dense-sampling design (N=3) , analogous to the rigorous small-N primate study designs and small-N human case studies to prioritize internal validity and depth of individual-level analysis[36,37].

Human consciousness is supported by integrated brain activity across functionally segregated areas[38]. Here we show that EC exhibits a distinctive reorganization of brain networks: higher brain activity in unimodal brain systems (VN, DAN), and temporal pol, lower activity in transmodal brain systems (DMN), as well as regions in the subcortex, brainstem, and cerebellum, expansion of the principal cortical gradient, enhancing segregation between unimodal and transmodal regions, and network–neurochemical coupling aligned with histaminergic H_3 receptor topography. Furthermore, spatial meta-analytic decoding associates the EC pattern with cognitive processes associated with perception/attention and reduced mental suffering and psychological

distress[39]. These results suggest a reconfiguration of the limbic network[40,41], consistent with meditators' post-EC reports and enduring psychological transformation of clarity, relief, and equanimity. These results offer novel insights into the neural correlates of EC, highlighting its potential to influence brain function as well as ultimately our understanding of consciousness and human flourishing, given the profound aftereffects reported.

Contrary to accounts that associate non-conscious states with global cortical suppression[42] and gradient flattening and widespread integration loss[43], EC showed higher local activity in unimodal sensory regions and reduced activity in transmodal regions and networks, specifically the DMN, and key subcortical and brainstem regions such as the caudate, thalamus, globus pallidus, and ventral tegmentum area. This reduced connectivity, notably in the basal ganglia[44-46] and brainstem[47] could be indicative of a indicating gating of access of sensation and percpetion[48] and wakefulness[47]. These findings partially mimic patients having disorders of consciousness, such as those with minimally conscious state and unresponsive wakefulness syndrome[49], who also demonstrated reduced brain activity in the DMN. In contrast, the principal gradient expands (unimodal values become more negative; transmodal values become more positive) and the distribution was flatter across all networks in EC, suggesting specialization of brain functions during EC. Unlike non-conscious states due to pharmacological interventions or disorders of consciousness, EC is endogenous, volitional, and followed by equanimity rather than disorientation. These contrasts support the view that multiple routes to non-conscious states exist, such as pharmacologic/global suppression versus selective decoupling, with divergent network consequences.

Two most prominent theories of consciousness are GNW and IIT. GNW posits that consciousness depends on long-range recurrent broadcast across frontoparietal hubs and non-consciousness accompanies reduced feedback and integration (e.g., anesthesia)[27]. EC is partly consistent with this view wherein DMN and thalamic suppression imply diminished recurrent broadcast to the workspace but constrains GNW because unimodal systems (VN/DAN) remain engaged and the principal gradient polarizes rather than collapses. Thus, selective decoupling of recurrent access to transmodal hubs, rather than frontoparietal shutdown, can suffice to suspend awareness. In contrast, IIT predicts that non-conscious states reflects reduced integration/differentiation, which often manifests empirically as flattened principal gradients and

loss of complex spatial modes in pharmacological interventions and disorders of consciousness[28,43,50]. EC shows the opposite pattern: gradient expansion, stronger unimodal–transmodal segregation in the absence of awareness, and reduced lower-order brain modes in EC. This directly challenges IIT, indicating that excessive segregation rather than loss off integration can also yield non-conscious states. Finally, according to AIF, loss of consciousness can arise from down-weighting the precision of sensory prediction errors[29]. Surprisingly, compared to GNW and IIT, EC supports AIF on multiple fronts. The reduced activity in the thalamus and brainstem together with increased activity in unimodal systems is consistent with precision gating. Additionally, network–neurochemical coupling to histamine H_3 receptor topography in unimodal cortex could explain neuromodulation on precision control[35]. Finlly, post-EC sensory clarity and equanimity is consistent with a transient precision overshoot, a brief increase in the gain assigned to sensory prediction errors which yields unusually vivid perception while self-referential priors remain down-weighted. In short, EC supports precision-gating (AIF), refines GNW by dissociating recurrent access from generic frontoparietal activity, and challenges IIT by demonstrating non-conscious states with increased hierarchical segregation rather than uniform flattening.

A unique contribution of this study is the link between EC and neurotransmitter receptor topography. Brain activity during EC co-varies with H_3 receptors receptor topography. As presynaptic autoreceptors and heteroreceptors, H_3 receptors regulate histamine release and suppress acetylcholine, dopamine, and norepinephrine, shaping arousal, attention, and sensory filtering[51-53]. EC's coupling to H_3-dense unimodal cortices and reduced engagement of transmodal hubs rich in $mGluR_5$/NMDA/D_1 may allow habitual cognitive constraints to relax, enabling underlying intrinsic brain dynamics to emerge[54] and modulate the type of conscious experience[55]. This shift likely allows practitioners to re-engage perception with heightened equanimity and reduced cognitive bias, providing optimal conditions for deep meditative insight. Notably, similar decreases in transmodal network activity have been observed during ACAM[2] and AIIM[56]. Upon exiting EC, unimodal networks enable a rapid, equanimous re-engagement of sensory processes, giving rise to the vivid clarity, equanimity, and deep insight into the phenomenology of the mind practitioners describe.

EC may be best understood as a "reset" of consciousness, in which self-referential loops are silenced, perceptual systems reorganized, and affective load attenuated. Thus, beyond the field

of cognitive neuroscience, EC offers a radical empirical model for advancing mental health, wellbeing, and human flourishing. The transformative aftereffects of EC—including deep sense of relief, clarity, equanimity, and reductions in repetitive thought, self-talk, and craving—map onto diminished self-referential processing and enhanced perceptual networks, according to the decoded meta-analytic cognitive maps from Neurosynth. These neural and experiential changes directly address components of psychological suffering[10]. Finally, the neural signatures of EC could serve as biomarkers for advanced meditation outcomes, guiding machine-learning-based personalization of practice[57] or neuromodulation protocols to target specific meditation outcomes, such as kindness, concentration, or acceptance[58]. Thus, EC point towards novel strategies for facilitating increasingly effective mental health interventions[59].

This study has considerable strengths including a whole-brain approach at high spatial resolution using ultra-high-resolution fMRI data with stringent methodological approaches. Nevertheless, there are several important limitations to consider. First, as this study is the first to investigate extended cessation, specifically EC, our results should be considered an initial step that should be replicated. While we compared EC to non-meditative states, a natural extension would be to compare EC to other meditative states to elucidate similarities and differences between EC and advanced forms of mediation. The absence of consciousness and self-reports during EC poses a challenge in understanding the subjective non-experience and its correlation with the neuroimaging findings. However, Neurosynth decoding offered robust evidence linking EC brain state to enhanced perceptual clarity, sensitivity, and the absence of mental suffering. These findings strongly suggest that significant brain reorganization occurs during EC to a degree that supports these subjective subsequent phenomena.

In conclusion, our results provide the first evidence for the neural correlates extended cessation. Extended cessation is marked by higher activity in unimodal regions with downregulation of transmodal and thalamic regions, expansion of cortical gradients, and reduced low-order global eigenmodes. Our results supports AIF, constraints GNW, and challenges IIT. These findings not only deepen our understanding of extended cessation but also illuminate fundamental mechanisms underlying human consciousness. More broadly, EC reveals a selective "reset" capacity of the mind that attenuates self-referential burden while sharpening perceptual

engagement, opening tractable neuromodulatory and behavioral routes to reduce suffering and advance human flourishing.

Materials and Methods

Participants

Participants were three male advanced meditators, Subject 2 (Male, age 32 at time of data collection), Subject 3 (age 46 at time of data collection), and Subject 4 (age 57 at time of data collection). Important to the current study, the participants are advanced meditators and reported being able to incline towards EC as the target of meditation. Subject 2 had over 19 years of meditation experience with total meditation experience of an estimated at least 15,000 hours. Subject 3 had over 4 years of meditation experience, and an estimated total practice amount at least of 9,000 hours. Subject 4 had over 50 years of meditation experience with total meditation experience of at least 10,000 hours. Lifetime practice hours are approximate self-reports based on duration and frequency of weekly practice and retreats. We also note that lifetime hours are not necessarily a direct measure of meditative expertise. The Mass General Brigham IRB approved the study, and the participants provided informed consent.

Experimental design

Extended cessation (EC)

FMRI data during EC was collected as part of a larger study of advanced meditation practices. In this advanced practice of EC, participants have trained extensively to develop the precision to enter and exit EC at specific, predefined times. This level of mastery reflects not only the ability to achieve a deep cessation state but also control over the duration and timing of the state. The participants performed EC meditation as the last meditation session after all other MRI sessions (structural scans, advanced concentrative absorption meditation, advanced insight meditation, non-meditative control conditions) were completed. The total amount of fMRI data collected for EC for each participant was approximately 45 minutes across three sessions. We asked the participant to meditate, enter, and maintain EC for 15 minutes during each session.

An EC run started with the participant making an intention to stay in EC for only 15 minutes. Then the participant started meditating at the start of the EC run. As some participants indicated that it was not possible for them to self-report entrance to this state, we did not attempt to mark when the participant entered EC. The run ended when the participant exited out of EC and indicated the exit with a button press. Retrospectively, we asked participants to estimate the duration it took them to enter EC if they did not indicate with a button press initially. After completing the meditation task, all participants completed a standardized EC phenomenology questionnaire—designed to reflect how they typically practice and experience EC—covering preparation, onset, absence of consciousness, exit, and afterglow. Two participants provided their phenomenology responses after data collection had formally concluded, and their delayed reports have been included in the dataset.

Non-meditative control conditions

We developed two non-meditative control conditions (hereon control conditions) that were used to compare against EC. These control conditions were designed to engage the participant's mind with non-meditative mental activities. These conditions were carefully selected to be sufficiently engaging to not induce meditative states. We did not use a resting-state control condition, since experienced meditators may enter meditative states during this period[60].

The two different control conditions implemented in this study were: (1) a memory control condition in which participants were asked to reminisce the events of the past two weeks and narrate them sub-vocally in their minds, closing their eyes and without moving their lips, for 8 minutes (min); and a (2) counting control condition, where the participants were asked to mentally count down in decrements of 5 from 10,000 for 8 min, closing their eyes and without moving their lips. We collected two runs for each control condition, which provided 16 mins data for each control condition. However, for participant ABC, only a single run for each control condition as part of another study.

Neuroimaging acquisition

Neuroimaging was acquired using a 7T MR scanner (SIEMENS MAGNETOM Terra) using a 32-channel head coil. Functional imaging was performed using a single-shot two-

438 dimensional echo planar imaging sequence with T2*-weighted BOLD-sensitive MRI, repetition
439 time (TR) = 2.9 sec, echo time (TE) = 30 ms, flip angle (FA) = 75°, field of view (FOV) = [189 x
440 255], matrix = [172 x 232], GRAPPA factor = 3, voxel size = 1.1 x 1.1 x 1.1 mm^3, 126 slices,
441 interslice distance = 0 mm, bandwidth = 1540 Hz/px, echo spacing = 0.75 ms. Slice acquisitions
442 were acquired for the whole brain, with interleaved slices, sagittal orientation, and anterior-to-
443 posterior phase encoding. Opposite phase-encoded (i.e., posterior-to-anterior) slices with the same
444 parameters were also acquired to perform distortion correction.

445 Whole-brain T1-weighted structural images were acquired as follows: TR = 2.53 sec, TE
446 = 1.65 ms, inversion time = 1.1 sec, flip angle = 7°, 0.8mm isotropic resolution, FOV = 240 x 240,
447 GRAPPA factor = 2, bandwidth = 1200 Hz/Px. The participant's physiological (i.e., heart rate
448 using pulse oximetry and respiration using breathing bellows) signal recordings were collected
449 throughout the scanning session.

450 Each neuroimaging session started each time the participant's position was localized in the
451 scanner and lasted until the next localization was conducted, usually after the participant left the
452 scanner to rest, typically after two hours.

453 **Neuroimaging preprocessing**

454 Preprocessing steps were conducted at the level of MRI session and for all runs within that
455 session, similar to our previous protocol, using AFNI[2]. Details of the preprocessing steps are
456 described in our previous study[2]. In short, steps consisted of (1) de-spiking; (2) RETROspective
457 Image CORrection (RETROICOR)[61] to regress out the effects of physiological (cardiac and
458 respiratory) noise on data; (3) slice time correction; (4) distortion correction using opposite phase-
459 encoded EPI; (5) motion correction; and (6) registering the anatomical dataset (T1) to a standard
460 (MNI152_2009) template. Additional preprocessing steps included: (7) scrubbing any volume
461 with motion > 0.3mm and had more than 5% outlier voxels; and (8) regressing out eroded
462 cerebrospinal fluid (CSF) mask time course and motion parameters (3 translations, 3 rotations) per
463 run, and band-pass filtering (0.01 – 0.1Hz). Each fMRI run was then segmented into one-minute
464 segments for statistical analyses, similar to our previous work on advanced meditation [2].

465 **Regions of interest (ROI)**

466 We used four different parcellation/segmentation schemes to define ROIs for subsequent
467 whole-brain analyses: (1) Schaefer-400 parcellation atlas for cortical areas[62]; (2) 34-region Tian
468 subcortex atlas for subcortical regions[63]; (3) 54 Bianciardi brainstem atlas[64]; and (4) 10 Multi-
469 Domain Task Battery (MDTB) functional cerebellar atlas[65]. In total our parcellation/segmentation
470 yielded 498 ROIs across the brain. For functional and effective connectivity analyses specifically,
471 we opted to use the Schaefer-100 parcellation atlas for cortical areas instead of the 400 parcellation
472 scheme[62] and the 16-region Tian subcortex atlas for subcortical regions[63]. This decision was made
473 to reduce the number of ROIs, thereby facilitating the interpretation of whole-brain effective
474 connectivity patterns and enabling direct comparability between functional and effective
475 connectivity results, while still maintaining a reasonably high spatial resolution for cortical
476 regions.

477 **Neuroimaging analyses**

478 ***Regional homogeneity analysis***

479 Regional homogeneity (ReHo) is a measure of similarity in temporal activation pattern of
480 a voxel and its nearby voxels[66]. This measure of local functional connectivity within brain regions
481 is a close derivative of underlying brain activity[66]. A higher ReHo value indicates stronger
482 synchronization of local brain regions, indicating greater functional connectivity in that region and
483 thus an index of greater brain activity. In this study, we defined a cluster size of 27 voxels and
484 calculated the ReHo values for each fMRI segment. We standardized the ReHo values before
485 smoothing the standardized ReHo maps using a 2 mm full-width half-maximum (FWHM) kernel.
486 The standardized ReHo values were then parcellated using the four different
487 parcellation/segmentation schemes[62-65], yielding 498 ReHo values for each fMRI segment.

488 ***Functional connectivity***

489 Data was smoothed using a 2 mm FWHM as we were interested in connectivity of smaller
490 brain regions such as the brainstem. Then for each segment, whole-brain time series of the 180
491 brain regions as defined previously was extracted, followed by computation of 180x180 functional
492 connectivity matrices using Pearson's correlation.

493 ***Effective connectivity: Regression dynamic causal modeling (rDCM)***

494 Whole-brain effective connectivity was assessed using regression dynamic causal
495 modeling (rDCM). rDCM, a variant of DCM for fMRI, enables effective connectivity analyses
496 across whole-brain networks with computational efficiency[67-71] without sacrificing reliability[72].
497 The validity of this procedure has been established in both task-based and resting-state fMRI
498 studies[67,68,70,72,73]. Specifically, rDCM incorporates modifications to DCM[72] including: (1)
499 translation of equations into the frequency domain using Fourier transformation; (2) replacement
500 of nonlinear hemodynamic models with linear functions; (3) mean-field approximation across
501 regions; and (4) specification of priors for neuronal parameters and noise precision. These
502 modifications transform linear DCM into Bayesian linear regression in the frequency domain,
503 which ultimately facilitates highly efficient DCM model inference[70,73].

504 To compute effective connectivity, preprocessed data at step 6 (normalization) was first
505 smoothed using a 2 mm FWHM. Time series of each ROI were then extracted after regressing out
506 6 motion parameters, white matter and CSF signals, with discrete cosine basis set with frequency
507 characteristics of resting-state brain dynamics (0.01– 0.1 Hz). Whole-brain effective connectivity
508 was then calculated using rDCM for resting-state fMRI[68] to examine whole-brain effective
509 connectivity[69,74-77]. First-level rDCM models for 180 ROIs were then computed using the rDCM
510 module within the Translational Algorithms for Psychiatry Advancing Science (TAPAS)
511 toolbox[78].

512 ***Principal gradient-mapping***

513 To map the gradients, we first computed a template gradient through a multi-step process.
514 First, data was smoothed using a 6 mm FWHM kernel, followed by computation of functional
515 connectivity matrices for each segment using the Schaefer 400-regions 7-network atlas using
516 Pearson's correlation, thus producing a 400×400 functional connectivity matrix. These individual
517 matrices were then averaged across all segments, resulting in a mean functional connectivity
518 matrix. Subsequently, gradients for this mean matrix were derived by thresholding the mean
519 correlation matrix at 90% sparsity to retain only the strongest connections, followed by generating
520 a similarity matrix using cosine similarity to capture the connectivity pattern similarities among
521 ROIs. The resulting similarity matrix served as input for the diffusion map embedding algorithm,

522 from which the principal gradients were extracted. We computed a template gradient from an out-
523 of-sample dataset of 134 subjects from the HCP dataset (the validation cohort used by[79]).

524 Following template gradient computation, alignment with individual segment gradients
525 was performed. The principal gradient values for each fMRI segment were computed based on
526 their respective functional connectivity matrices and then aligned with the template gradient using
527 Procrustes rotations with 10 iterations to ensure optimal comparison across datasets. All analyses
528 described herein were conducted using the BrainSpace toolbox implemented in Python[79]. Using
529 the gradient values obtained from gradient alignment, we computed the average network gradient
530 values for each network by averaging the gradient values of all the parcels within that network.

531 ***Cortical dynamics: Geometric eigenmodes***

532 To decompose fMRI activity into 200 frequency-specific eigenmodes, we used geometric
533 eigenmodes derived from a population-averaged midsurface thickness template of the neocortical
534 surface from Pang et al., wherein the methods to generate these geometric eigenmode templates
535 are also described[80]. Briefly, the geometric eigenmodes were computed by constructing the
536 Laplace-Beltrami operator from the cortical mesh and solving the eigenvalue problem. The
537 resulting eigenvalues are ordered according to spatial frequency/wavelength of each mode, where
538 mode 1 has the longest wavelength (lowest frequency) while higher modes have shorter
539 wavelengths (higher frequency). Conversely, eigenmodes are the complete basis set—a weighted
540 sum of varying-wavelength modes. Lower-numbered modes capture large-scale spatial patterns
541 (e.g. left/right hemisphere, anterior/posterior regions) while higher-number modes correspond to
542 smaller-scale spatial patterns where functional properties of nearby regions vary independent of
543 proximity.

544 Using the geometric eigenmodes, we decomposed functional MRI data to reveal emerging
545 cortical spatiotemporal dynamic patterns by examining the contribution of each eigenmode to the
546 cortical activity at each time instance. At each time point of each fMRI time courses, fMRI data
547 were projected onto each of the 200 geometric eigenmodes, yielding the temporal activity of the
548 particular eigenmode in a method described previously[81,82]. Subsequently, the temporal activation
549 of eigenmodes were analyzed in terms of their power (the strength of an eigenmode's activation
550 at a given fMRI time instance: $|\omega_k(t_i)|$) and energy (the eigenmode's frequency-weighted

contribution, estimated by weighting the square of the eigenmode's strength of activation by the square of its corresponding eigenvalue (λ_k) at each time point: $|\omega_k(t_i)|^2 \lambda_k^2$) at each fMRI time point. Mean power and energy were calculated by averaging the power and energy of each eigenmode across all time points in a single segment (i.e. yielding 200 mean power and energy values for 200 modes per fMRI segment). Maximum power and energy were calculated as the maximum spectra value for a given eigenmode across all time points within a segment (i.e. yielding 200 maximum power and energy values for 200 modes per fMRI segment). Unless otherwise noted, all reported maximum and mean power and energy values are reported on a log-scale[82]. Brain total power and total energy were computed by summing power and energy across all eigenmodes for each time point and then averaging all time points within a segment.

Influence of neurotransmitter systems receptor density: Positron Emission Tomography (PET) neurotransmitter systems receptor density maps

We used a recently made available public neurotransmitter systems receptor density maps for 19 receptors and transporters, across 9 neurotransmitter systems by Hansen and colleagues at https://github.com/netneurolab/hansen_receptors[35]. These include dopamine (D_1, D_2, DAT) noradrenaline (NAT), serotonin(5-HT_{1A}, 5-HT_{1B}, 5-HT_{2A}, 5-HT_4, 5-HT_6, 5-HTT), acetylcholine ($\alpha_4\beta_2$, M_1, VAChT), glutamate ($mGluR_5$, NMDA), GABA ($GABA_A$), histamine (H_3), cannabinoid (CB_1), and opioid (MOR) receptors. Details regarding the neurotransmitter systems receptor density maps, each PET dataset, and their respective acquisition and limitations can be found in ref[35]. Volumetric PET images were registered to the MNI-ICBM 152 nonlinear 2009 (version c, asymmetric) template, averaged across participants within each study, and then parcellated and receptors/transporters with more than one mean image of the same tracer were combined using a weighted average[35].

Decoding of brain activity using data-driven Neurosynth cognitive maps

To provide a complementary approach for analyzing brain activity patterns with behavior in the absence of behavioral data, we examined the spatial similarity of ReHo maps with 123 meta-analytic brain maps derived from the Neurosynth database. Neurosynth generates probabilistic measurements that can be interpreted as a quantitative representation of the association between regional fluctuations in activity and psychological processes. Although Neurosynth's database

contains over 1,000 terms, we narrowed our focus to terms related to cognition and behavior, drawing from previous research[35,83,84]. Our selected set of 123 terms encompasses broad categories, ranging from attention and emotion, to more specific processes such as visual attention and episodic memory. The terms also include basic behaviors (e.g., eating and sleep) and emotional states (e.g., fear and anxiety).

Statistical analysis

ReHo brain activity

Linear mixed-effects models were used to analyze ReHo differences between EC and control conditions. The model included task condition as a fixed effect and random intercepts for participant and for segments nested within subject. Corrections for multiple comparisons across models were applied using false-discovery rate (FDR) across all 498 ROIs. We used Dunnett's test to compare the difference between EC and control tasks, with EC as the reference group controlling for multiple comparisons using Bonferroni correction for k = 2 comparisons. For ease of interpretation, all coefficients were flipped to retrieve the contrast of EC against the control conditions. Analyses were conducted in *R*[85] loading on R Studio v2022.12.0.353.20[86].

Functional connectivity: Network-based statistics (NBS)

NBS was used to explore functional connectivity differences between EC and control conditions in the whole-brain network containing 198 nodes and 19,503 ($\frac{198*197}{2}$) unique edges[87]. NBS is a nonparametric statistical method used to perform mass-univariate statistical tests for multiple graph comparisons. NBS identifies interconnected subnetworks exhibiting significant differences in functional connectivity between groups or conditions. Instead of treating connections independently, NBS leverages the inherent interconnectedness of the brain by identifying clusters of connections collectively differing across groups. This enables sensitive detection of subtle yet interconnected alterations in whole-brain functional connectivity. T-scores were computed for each pairwise connection under contrasts EC > control and EC < control separately, with additional separate analyses for counting and memory control conditions. Each test was conducted at the primary threshold ($t = 3.1$, $p = 0.025$) to select the suprathreshold connections for which the t-scores exceeded the primary t-value. We used $p = 0.025$ to

accommodate two contrasts per control comparison (EC > control and EC < control). Connected components where the EC showed higher or lower functional connectivity than the control conditions were identified, and the number of the edges or their size was stored. A permutation test was then performed to determine the significance of each component by comparing its size to the distribution of maximum component sizes under random group assignments (5000 permutations). Corrected p-values were computed as the proportion of permutations with larger maximum components than the observed size. NBS enabled sensitive detection of interconnected functional connectivity alterations in EC by leveraging the inherent network structure of the brain and rigorously accounting for multiple comparisons.

Effective connectivity: Directed network-based statistics (dNBS)

dNBS, an extension of NBS, was used to analyze effective connectivity differences between EC and control conditions. We investigated two contrast, EC > control and EC < control separately, with additional separate analyses for counting and memory control conditions. The statistical significance of the outcomes was determined using a primary threshold of $t = 3.1$ ($p = 0.025$) and 5000 permutations, following the same procedures as in the conventional NBS approach. The key distinction between dNBS and NBS lies in the fact that dNBS analyzes twice the number of edges compared to NBS, accommodating the directional nature of effective connectivity measures.

Brain organization: Connectivity gradients

Linear mixed-effects models were used to analyze cortical principal gradient differences between EC and control conditions. These tests were performed at both the network-level, encompassing 7 cortical networks, and at the ROI-level, comprising 400 ROIs. This dual approach allowed for a robust examination of gradient variations across different scales of cortical organization. Corrections for multiple comparisons were applied using false-discovery rate across the 7 networks and 400 ROIs respectively.

Cortical dynamics of EC: Geometric eigenmode power and energy

To analyze differences in frequency-specific eigenmode mean power and energy between EC and control conditions while minimizing multiple comparisons, we utilized 15 eigengroups:

grouping of eigenmodes according to spatial frequency[80,88]. Eigengroups provide a way to aggregate degenerate solutions from the solving of the eigendecomposition such that eigenmodes with the same number of nodal lines and wavelengths are grouped together. This method allows for investigation of eigenmode metrics that are less affected by noise[89,90]. Using this approach, each eigengroup's power and energy were then compared as reference values to both counting and memory control conditions using linear mixed-effects models. The resulting *p*-values were FDR corrected across both control condition comparisons. Finally, linear regression was used to examine mean power and energy differences between EC and control conditions.

Influence of neurotransmitter systems receptor density: Partial least squares correlation

We used partial least squares correlation (PLSC) analysis to explore the multivariate relationship between neurotransmitter systems receptor densities and EC delta-weighted-degree connectivity maps. PLSC is an unsupervised multivariate statistical technique that decomposes two datasets into orthogonal sets of latent variables with the goal of maximizing covariance between them[91]. In this context, the latent variables consist of receptor weights, EC-control weighted-degree weights and a singular value that represents the covariance between receptor distributions and weighted-degree connectivity that is explained by the latent variable.

NS delta-weighted-degree maps were created by first thresholding all negative-weighted connectivity and self-connections to zero, followed by summing each region's positive connection weights to all other regions. we only use cortical atlas for this analysis, similar to previous research on chemoarchitecture of the brain[35,83]. Segment-level weighted-degree vectors were then averaged across all segments within each task, producing a single weighted-degree profile per participant per task. For each participant, the delta-weighted-degree map was calculated as the difference between EC and each control task, i.e., EC-Counting, and EC-memory. Finally, participant-level delta-weighted-degree profiles were then averaged across the three participants to obtain the two delta-weighted-degree maps, EC-Counting, and EC-memory.

By projecting the original receptor density and weighted-degree data onto the corresponding latent variable weights, we computed receptor and EC-difference scores, assigning each brain region a specific score for both. Receptor loadings were then calculated as the Pearson correlation between neurotransmitter systems receptor densities and receptor scores, with a similar

process used to compute EC-difference loadings (weighted-degree map and EC-difference scores). Importantly, PLSC does not (1) infer causal links between receptors and EC, (2) establish univariate associations between specific receptors and EC, or (3) rule out the possibility of additional connections between receptors and EC.

We assessed the significance of each latent variable's singular value using permutation spin-testing[92-94]. For each map, parcel coordinates were projected onto the spherical surface and then randomly rotated and original parcels were reassigned the value of the closest rotated parcel (10,000 repetitions)[95]. In addition to preserving the distribution of cortical values, this null model also preserves the spatial autocorrelation present in the data.

Contextualization of brain activity with Neurosynth cognitive maps

We used the *continuous.CorrelationDecoder* function from the NiMARE python package to contextualization of brain activity with Neurosynth cognitive maps[96]. We first fetched Neurosynth dataset and converted it to NiMARE dataset. Following, we retrieved the 123 cognitive terms from the database. We also computed delta-ReHo maps (EC-counting, and EC-memory) for decoding. Finally, we used the *CorrelationDecoder* function to decode the association between the unthresholded delta-ReHo maps and cognitive maps.

References

1 Seth, A. K. & Bayne, T. Theories of consciousness. *Nat Rev Neurosci* **23**, 439-452 (2022). https://doi.org:10.1038/s41583-022-00587-4

2 Yang, W. F. Z. *et al.* Intensive whole-brain 7T MRI case study of volitional control of brain activity in deep absorptive meditation states. *Cerebral Cortex* **34**, bhad408 (2024).

3 Chowdhury, A. *et al.* Multimodal neurophenomenology of advanced concentration absorption meditation: An intensively sampled case study of Jhana. *Neuroimage* **305**, 120973 (2025).

4 Chowdhury, A. *et al.* Investigation of advanced mindfulness meditation "cessation" experiences using EEG spectral analysis in an intensively sampled case study. *Neuropsychologia* **190**, 108694 (2023).

5 van Lutterveld, R., Cahaly, T., Ingram, D. & Sacchet, M. D. Brain criticality and advanced meditation “cessation” events: An intensively sampled electroencephalography case study. *SSRN* (2025). https://doi.org:10.2139/ssrn.5296987

6 Berkovich-Ohana, A. A case study of a meditation-induced altered state: increased overall gamma synchronization. *Phenomenology and the Cognitive Sciences* **16**, 91-106 (2015).

7 van Lutterveld, R., Chowdhury, A., Ingram, D. M. & Sacchet, M. D. Neurophenomenological Investigation of Mindfulness Meditation "Cessation" Experiences Using EEG Network Analysis in an Intensively Sampled Adept Meditator. *Brain Topogr* (2024).

8 Laukkonen, R. E. *et al.* Cessations of consciousness in meditation: Advancing a scientific understanding of nirodha samāpatti. *Progress in Brain Research* **280**, 61-87 (2023).

9 Sacchet, M. D., Fava, M. & Garland, E. L. Modulating self-referential processing through meditation and psychedelics: Is scientific investigation of self-transcendence clinically relevant? *World Psychiatry* **23**, 298-299 (2024).

10 Sparby, T. & Sacchet, M. D. The Third Wave of Meditation and Mindfulness Research and Implications for Challenging Experiences: Negative Effects, Transformative Psychological Growth, and Forms of Happiness. *Mindfulness* (2025). https://doi.org:10.1007/s12671-025-02607-7

11 Wright, M. J., Sanguinetti, J. L., Young, S. & Sacchet, M. D. Uniting contemplative theory and scientific investigation: Toward a comprehensive model of the mind. *Mindfulness* **14**, 1088–1101 (2023).

12 Galante, J. *et al.* A framework for the empirical investigation of mindfulness meditative development. *Mindfulness* **14**, 1054–1067 (2023).

13 Amaro, A. Realization Is Here and Now. *Mindfulness* **12**, 795-797 (2020). https://doi.org:10.1007/s12671-020-01526-z

14 Anālayo, B. The Four Levels of Awakening. *Mindfulness* **12**, 831-840 (2020). https://doi.org:10.1007/s12671-020-01530-3

15 Rose, K. *Yoga, Meditation, and Mysticism: Contemplative Universals and Meditative Landmarks*. (Bloomsbury Academic, 2016).

16 Toan, L. N. Salvation, Enlightenment and Awakening in Shaping Followers' Perception and Understanding of Their Faith: A Linguistic Exploration. *International Journal of Religion* **5**, 286-299 (2024). https://doi.org:10.61707/mvedkv66

17 Sandilands, O. & Ingram, D. M. Documenting and defining emergent phenomenology: theoretical foundations for an extensive research strategy. *Front Psychol* **15**, 1340335 (2024). https://doi.org:10.3389/fpsyg.2024.1340335

18 Wright, M. J., Cha, V. L., Streifert, M. R., Ingram, D. M. & Sacchet, M. D. Risk Factors for Emergence of Sudden Unusual Mental or Somatic Experiences and Subsequent Suffering. *Clinical Psychological Science* (2025).

19 Wright, M. J. *et al.* Altered States of Consciousness are Prevalent and Insufficiently Supported Clinically: A Population Survey. *Mindfulness* **15**, 1162-1175 (2024). https://doi.org:10.1007/s12671-024-02356-z

20 Pujol, J. *et al.* Largest scale dissociation of brain activity at propofol-induced loss of consciousness. *Sleep* **44** (2021). https://doi.org:10.1093/sleep/zsaa152

21 Pujol, J. *et al.* Mapping the neural systems driving breathing at the transition to unconsciousness. *Neuroimage* **246**, 118779 (2022). https://doi.org:10.1016/j.neuroimage.2021.118779

22 Noriaki, H. Nirodhasamapatti-Its Historical Meaning in the Vijñaptimatrata System. *Indogaku Bukkyōgaku kenkyū* **23**, 1084-1074 (n.d.).

23 Gunaratana, M. H. *The Path of Serenity and Insight*. (Motilal Banarsidass, 1985).

24 Nanamoli, B. & Bodhi, B. *The Middle Length Discourses of the Buddha: A Translation of the Majjhima Nikāya*. (Wisdom Publications, 2009).

25 Griffiths, P. J. *On being mindless : Buddhist meditation and the mind-body problem*. (Open Court, 1986).

26 Lusthaus, D. *Buddhist Phenomenology : a Philosophical Investigation of Yogacara Buddhism and the Ch'eng Wei-shih Lun*. (RoutledgeCurzon, 2002).

27 Mashour, G. A., Roelfsema, P., Changeux, J. P. & Dehaene, S. Conscious Processing and the Global Neuronal Workspace Hypothesis. *Neuron* **105**, 776-798 (2020). https://doi.org:10.1016/j.neuron.2020.01.026

28 Tononi, G., Boly, M., Massimini, M. & Koch, C. Integrated information theory: from consciousness to its physical substrate. *Nat Rev Neurosci* **17**, 450-461 (2016). https://doi.org:10.1038/nrn.2016.44

29 Parr, T., Pezzulo, G. & Friston, K. J. *Active Inference: The Free Energy Principle in Mind, Brain, and Behavior*. (The MIT Press, 2022).

30 Girn, M. *et al.* Serotonergic psychedelic drugs LSD and psilocybin reduce the hierarchical differentiation of unimodal and transmodal cortex. *Neuroimage* **256**, 119220 (2022).

31 Margulies, D. S. *et al.* Situating the default-mode network along a principal gradient of macroscale cortical organization. *Proc Natl Acad Sci U S A* **113**, 12574-12579 (2016).

32 Timmermann, C. *et al.* Human brain effects of DMT assessed via EEG-fMRI. *Proc Natl Acad Sci U S A* **120**, e2218949120 (2023). https://doi.org:10.1073/pnas.2218949120

33 Zhang, H. *et al.* Cortical connectivity gradients and local timescales during cognitive states are modulated by cognitive loads. *Brain Struct Funct* **227**, 2701-2712 (2022). https://doi.org:10.1007/s00429-022-02564-0

34 Zhang, J. *et al.* Intrinsic Functional Connectivity is Organized as Three Interdependent Gradients. *Sci Rep* **9**, 15976 (2019). https://doi.org:10.1038/s41598-019-51793-7

35 Hansen, J. Y. *et al.* Mapping neurotransmitter systems to the structural and functional organization of the human neocortex. *Nat Neurosci* **25**, 1569-1581 (2022). https://doi.org:10.1038/s41593-022-01186-3

36 Becker, A. The benefits of single-subject research designs and multi-methodological approaches for neuroscience research. *Front Hum Neurosci* **17**, 1190412 (2023). https://doi.org:10.3389/fnhum.2023.1190412

37 Milne, A. E., Petkov, C. I. & Wilson, B. Auditory and Visual Sequence Learning in Humans and Monkeys using an Artificial Grammar Learning Paradigm. *Neuroscience* **389**, 104-117 (2018). https://doi.org:10.1016/j.neuroscience.2017.06.059

38 Alkire, M. T., Hudetz, A. G. & Tononi, G. Consciousness and anesthesia. *Science* **322**, 876-880 (2008).

39 Yang, W. F. Z., Chowdhury, A., Sparby, T. & Sacchet, M. D. Deconstructing the self and reshaping perceptions: An intensive whole-brain 7T MRI case study of the stages of insight during advanced investigative insight meditation. *NeuroImage*, 120968 (In press).

40 Herlin, B., Navarro, V. & Dupont, S. The temporal pole: From anatomy to function-A literature appraisal. *J Chem Neuroanat* **113**, 101925 (2021). https://doi.org:10.1016/j.jchemneu.2021.101925

41 Ralph, M. A., Jefferies, E., Patterson, K. & Rogers, T. T. The neural and computational bases of semantic cognition. *Nat Rev Neurosci* **18**, 42-55 (2017). https://doi.org:10.1038/nrn.2016.150

42 Tanabe, S. *et al.* Altered Global Brain Signal during Physiologic, Pharmacologic, and Pathologic States of Unconsciousness in Humans and Rats. *Anesthesiology* **132**, 1392-1406 (2020). https://doi.org:10.1097/ALN.0000000000003197

43 Huang, Z., Mashour, G. A. & Hudetz, A. G. Functional geometry of the cortex encodes dimensions of consciousness. *Nat Commun* **14**, 72 (2023). https://doi.org:10.1038/s41467-022-35764-7

44 Seo, J., Kim, D. J., Choi, S. H., Kim, H. & Min, B. K. The thalamocortical inhibitory network controls human conscious perception. *Neuroimage* **264**, 119748 (2022). https://doi.org:10.1016/j.neuroimage.2022.119748

45 Wolff, M., Morceau, S., Folkard, R., Martin-Cortecero, J. & Groh, A. A thalamic bridge from sensory perception to cognition. *Neuroscience and Biobehavioral Reviews* **120**, 222-235 (2021). https://doi.org:10.1016/j.neubiorev.2020.11.013

46 Redinbaugh, M. J. & Saalmann, Y. B. Contributions of basal ganglia circuits to perception, attention, and consciousness. *Journal of Cognitive Neuroscience* **36**, 1620-1642 (2024).

47 Edlow, B. L. *et al.* Multimodal MRI reveals brainstem connections that sustain wakefulness in human consciousness. *Science Translational Medicine* **16**, eadj4303 (2024).

48 Redinbaugh, M. J. & Saalmann, Y. B. Contributions of Basal Ganglia Circuits to Perception, Attention, and Consciousness. *Journal of Cognitive Neuroscience* **36**, 1620–1642 (2024). https://doi.org:10.1162/jocn_a_02177pathways

49 Wang, Y. *et al.* Regional Homogeneity Alterations in Patients with Impaired Consciousness. An Observational Resting-State fMRI Study. *Neuroradiology* **64**, 1391-1399 (2022). https://doi.org:10.1007/s00234-022-02911-2

50 Luppi, A. I. *et al.* Distributed harmonic patterns of structure-function dependence orchestrate human consciousness. *Commun Biol* **6**, 117 (2023).

51 Lin, J. S., Sergeeva, O. A. & Haas, H. L. Histamine H3 receptors and sleep-wake regulation. *J Pharmacol Exp Ther* **336**, 17-23 (2011). https://doi.org:10.1124/jpet.110.170134

52 Yu, X., Franks, N. P. & Wisden, W. Sleep and Sedative States Induced by Targeting the Histamine and Noradrenergic Systems. *Front Neural Circuits* **12**, 4 (2018). https://doi.org:10.3389/fncir.2018.00004

53 Esbenshade, T. A. *et al.* The histamine H3 receptor: an attractive target for the treatment of cognitive disorders. *Br J Pharmacol* **154**, 1166-1181 (2008). https://doi.org:10.1038/bjp.2008.147

54 Tal, H., Wright, M., Prest, S., Sandved-Smith, L. & Sacchet, M. D. Active inference, computational phenomenology, and advanced meditation: Toward the formalization of the experience of meditation. *PsyArXiv* (2025). https://doi.org:10.31234/osf.io/pm5y2_v2

55 Zilles, K., Bacha-Trams, M., Palomero-Gallagher, N., Amunts, K. & Friederici, A. D. Common molecular basis of the sentence comprehension network revealed by neurotransmitter receptor fingerprints. *Cortex* **63**, 79-89 (2015). https://doi.org:10.1016/j.cortex.2014.07.007

56 Yang, W. F. Z., Chowdhury, A., Sparby, T. & Sacchet, M. D. Deconstructing the self and reshaping perceptions: An intensive whole-brain 7T MRI case study of the stages of insight during advanced investigative insight meditation. *Neuroimage* **305**, 120968 (2025).

57 Guidotti, R. *et al.* Long-Term and Meditation-Specific Modulations of Brain Connectivity Revealed Through Multivariate Pattern Analysis. *Brain Topogr* **36**, 409-418 (2023). https://doi.org:10.1007/s10548-023-00950-3

58 Sezer, I., Pizzagalli, D. A. & Sacchet, M. D. Resting-state fMRI functional connectivity and mindfulness in clinical and non-clinical contexts: A review and synthesis. *Neuroscience and Biobehavioral Reviews* **135**, 104583 (2022).

59 Abellaneda-Perez, K., Potash, R. M., Pascual-Leone, A. & Sacchet, M. D. Neuromodulation and meditation: A review and synthesis toward promoting well-being and understanding consciousness and brain. *Neurosci Biobehav Rev* **166**, 105862 (2024). https://doi.org:10.1016/j.neubiorev.2024.105862

60 Tang, Y. Y., Rothbart, M. K. & Posner, M. I. Neural correlates of establishing, maintaining, and switching brain states. *Trends in Cognitive Sciences* **16**, 330-337 (2012).

61 Glover, G. H., Li, T. Q. & Ress, D. Image-based method for retrospective correction of physiological motion effects in fMRI: RETROICOR. *Magnetic Resonance in Medicine* **44**, 162-167 (2000).

62 Schaefer, A. *et al.* Local-Global Parcellation of the Human Cerebral Cortex from Intrinsic Functional Connectivity MRI. *Cerebral Cortex* **28**, 3095-3114 (2018).

63 Tian, Y., Margulies, D. S., Breakspear, M. & Zalesky, A. Topographic organization of the human subcortex unveiled with functional connectivity gradients. *Nature Neuroscience* **23**, 1421-1432 (2020).

64 Bianciardi, M. *et al.* In vivo functional connectome of human brainstem nuclei of the ascending arousal, autonomic, and motor systems by high spatial resolution 7-Tesla fMRI. *MAGMA* **29**, 451-462 (2016).

65 King, M., Hernandez-Castillo, C. R., Poldrack, R. A., Ivry, R. B. & Diedrichsen, J. Functional boundaries in the human cerebellum revealed by a multi-domain task battery. *Nature Neuroscience* **22**, 1371-1378 (2019).

66 Zang, Y., Jiang, T., Lu, Y., He, Y. & Tian, L. Regional homogeneity approach to fMRI data analysis. *Neuroimage* **22**, 394-400 (2004).

67 Frassle, S. *et al.* A generative model of whole-brain effective connectivity. *Neuroimage* **179**, 505-529 (2018). https://doi.org:10.1016/j.neuroimage.2018.05.058
68 Frassle, S. *et al.* Regression DCM for fMRI. *Neuroimage* **155**, 406-421 (2017).
69 Friston, K. J., Harrison, L. & Penny, W. Dynamic causal modelling. *Neuroimage* **19**, 1273-1302 (2003).
70 Frassle, S. *et al.* Whole-brain estimates of directed connectivity for human connectomics. *Neuroimage* **225**, 117491 (2021).
71 Razi, A. *et al.* Large-scale DCMs for resting-state fMRI. *Network Neuroscience* **1**, 222-241 (2017).
72 Frassle, S. & Stephan, K. E. Test-retest reliability of regression dynamic causal modeling. *Netw Neurosci* **6**, 135-160 (2022).
73 Frassle, S. *et al.* Regression dynamic causal modeling for resting-state fMRI. *Hum Brain Mapp* **42**, 2159-2180 (2021). https://doi.org:10.1002/hbm.25357
74 Friston, K. J. Functional and effective connectivity: a review. *Brain Connect* **1**, 13-36 (2011).
75 Friston, K. J., Kahan, J., Biswal, B. & Razi, A. A DCM for resting state fMRI. *Neuroimage* **94**, 396-407 (2014).
76 Friston, K. J. *et al.* Bayesian model reduction and empirical Bayes for group (DCM) studies. *Neuroimage* **128**, 413-431 (2016).
77 Razi, A., Kahan, J., Rees, G. & Friston, K. J. Construct validation of a DCM for resting state fMRI. *Neuroimage* **106**, 1-14 (2015).
78 Frassle, S. *et al.* TAPAS: An Open-Source Software Package for Translational Neuromodeling and Computational Psychiatry. *Front Psychiatry* **12**, 680811 (2021). https://doi.org:10.3389/fpsyt.2021.680811
79 Vos de Wael, R. *et al.* BrainSpace: a toolbox for the analysis of macroscale gradients in neuroimaging and connectomics datasets. *Commun Biol* **3**, 103 (2020). https://doi.org:10.1038/s42003-020-0794-7
80 Pang, J. C. *et al.* Geometric constraints on human brain function. *Nature* **618**, 566-574 (2023). https://doi.org:10.1038/s41586-023-06098-1
81 Atasoy, S., Donnelly, I. & Pearson, J. Human brain networks function in connectome-specific harmonic waves. *Nature Communications* **7**, 10340 (2016).
82 Atasoy, S. *et al.* Connectome-harmonic decomposition of human brain activity reveals dynamical repertoire re-organization under LSD. *Scientific Reports* **7**, 17661 (2017).
83 Luppi, A. I. *et al.* In vivo mapping of pharmacologically induced functional reorganization onto the human brain's neurotransmitter landscape. *Science Advances* **9**, eadf8332 (2023). https://doi.org:doi:10.1126/sciadv.adf8332
84 Yarkoni, T., Poldrack, R. A., Nichols, T. E., Van Essen, D. C. & Wager, T. D. Large-scale automated synthesis of human functional neuroimaging data. *Nature Methods* **8**, 665-670 (2011). https://doi.org:10.1038/nmeth.1635
85 R: A Language and Environment for Statistical Computing (R Foundation for Statistical Computing, Vienna, Austria, 2022).
86 RStudio: Integrated Development Environment for R (Posit Software, PBC http://www.posit.co, Boston, MA, 2022).
87 Zalesky, A., Fornito, A. & Bullmore, E. T. Network-based statistic: identifying differences in brain networks. *Neuroimage* **53**, 1197-1207 (2010). https://doi.org:10.1016/j.neuroimage.2010.06.041

88 Chen, Y.-C. *et al.* The individuality of shape asymmetries of the human cerebral cortex. *eLife* **11**, e75056 (2022). https://doi.org:10.7554/eLife.75056

89 Cao, T. *et al.* Mode-based morphometry: A multiscale approach to mapping human neuroanatomy. *Human Brain Mapping* **45**, e26640 (2024). https://doi.org:https://doi.org/10.1002/hbm.26640

90 Boyes, A. *et al.* Geometric eigenmode brain fingerprinting and its longitudinal associations with adolescent mental health and wellbeing. *bioRxiv*, 2024.2008.2008.607260 (2024). https://doi.org:10.1101/2024.08.08.607260

91 Krishnan, A., Williams, L. J., McIntosh, A. R. & Abdi, H. Partial Least Squares (PLS) methods for neuroimaging: a tutorial and review. *Neuroimage* **56**, 455-475 (2011). https://doi.org:10.1016/j.neuroimage.2010.07.034

92 Alexander-Bloch, A. F. *et al.* On testing for spatial correspondence between maps of human brain structure and function. *Neuroimage* **178**, 540-551 (2018). https://doi.org:10.1016/j.neuroimage.2018.05.070

93 Markello, R. D. & Misic, B. Comparing spatial null models for brain maps. *Neuroimage* **236**, 118052 (2021). https://doi.org:10.1016/j.neuroimage.2021.118052

94 Vasa, F. & Misic, B. Null models in network neuroscience. *Nat Rev Neurosci* **23**, 493-504 (2022). https://doi.org:10.1038/s41583-022-00601-9

95 Vazquez-Rodriguez, B. *et al.* Gradients of structure-function tethering across neocortex. *Proc Natl Acad Sci U S A* **116**, 21219-21227 (2019). https://doi.org:10.1073/pnas.1903403116

96 Salo, T. *et al.* NiMARE: neuroimaging meta-analysis research environment. *Aperture Neuro* **3**, 1-32 (2023). https://doi.org:10.52294/001c.87681

Author contributions

Conceptualization: MDS; Funding Acquisition: MDS; Methodology: MDS, TS; Data Collection: MDS, TS, RP, WFZY; Software: WFZY, GM, IB, RP; Formal Analysis: WFZY, AK, KA, GM, IB; Writing – Original Draft: WFZY and MDS; Writing – Review & Editing: WFZY, MDS, AK, KA, RP, and TS.

Funding information

Dr. Sacchet and the Meditation Research Program are supported by the Dimension Giving Fund, Tan Teo Charitable Foundation, and additional individual donors. Dr. Abellaneda-Pérez was financially supported by a Juan de la Cierva research grant (FJC2021-047380-I) of the Spanish Ministry of Science and Innovation. Dr. Terje Sparby is supported by Software AG Stiftung.

Competing interests

All authors declare no competing interests.

Data and materials availability

Data may be requested from the corresponding author and is subject to the Massachusetts General Hospital Institutional Review Board's guidelines and approval. All code used in this study may be made available by request from the corresponding author.

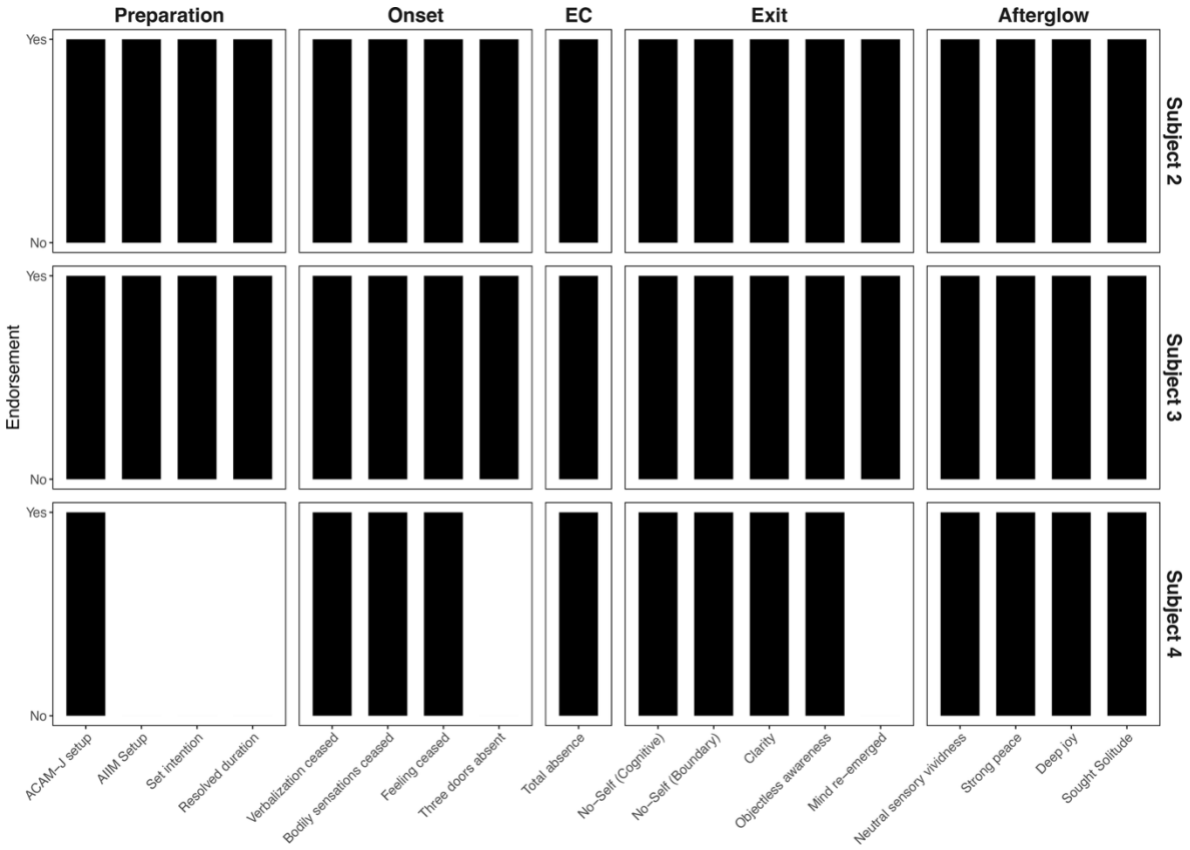

Fig. 1. Endorsement of EC phenomenology for each participant. Participants all endorsed the phenomenological items of EC presented here, except Subject 4. Although previously trained to set up EC using ACAM-J, Subject 4 had since developed an alternative approach and no longer required ACAM-J for setup. As such, the phenomenology for various components throughout EC differ slightly for Subject 4. ACAM-J = Advanced concentration absorption meditation-jhana, AIIM = advanced investigative insight meditation

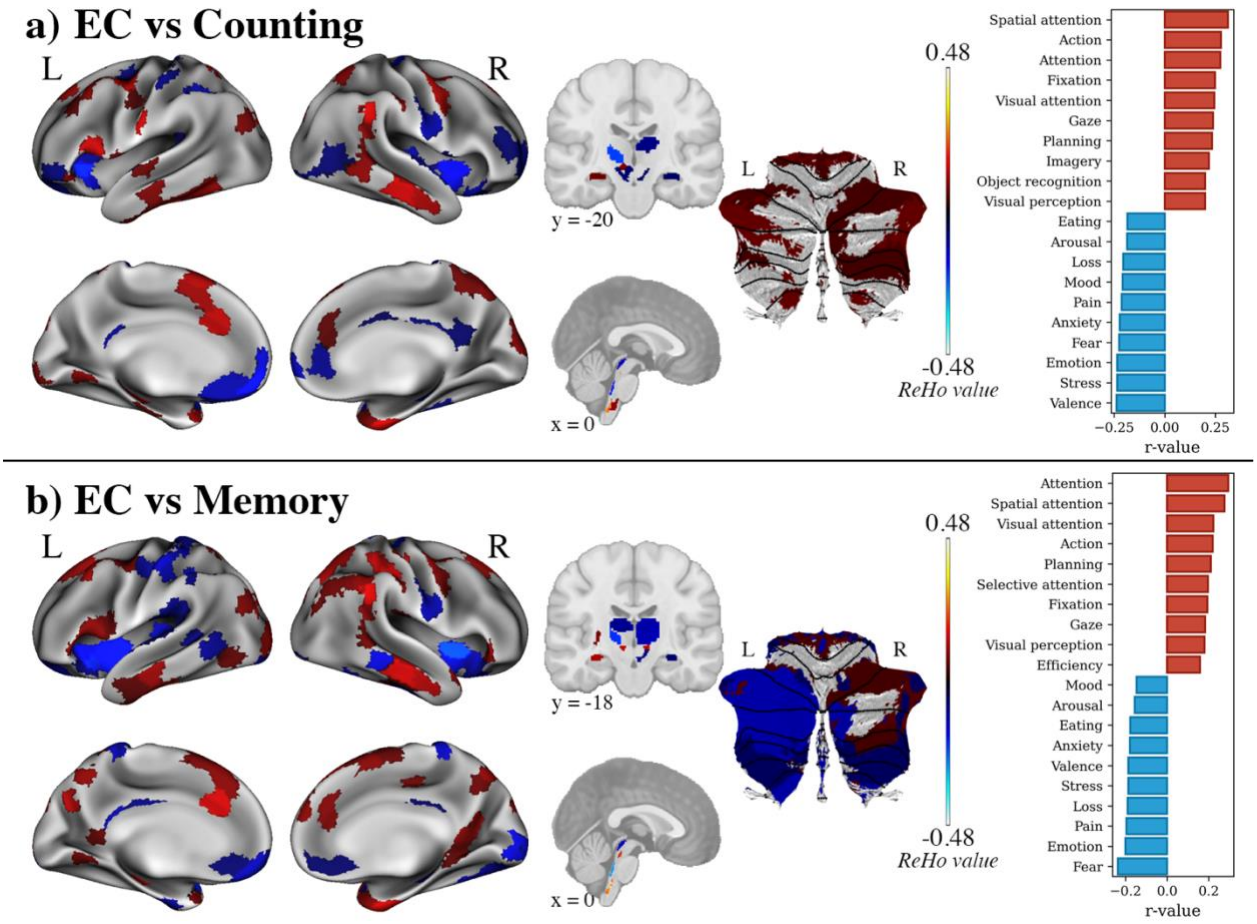

Fig. 2. Differences in regional homogeneity values (ReHo) between EC and control conditions. (a) EC, compared to the counting control condition, demonstrated increased ReHo values in the bilateral visual, posterior, temporal regions, parts the brainstem, and cerebellum, and decreased ReHo in bilateral prefrontal regions and posterior cingulate cortex, largely associated with the default-mode network. Subcortical activity reveals decreased ReHo values across the caudate, thalamus, globus pallidus, amygdala, and brainstem. **(b)** Similarly, compared to the memory condition, EC displayed increased ReHo values in bilateral visual, posterior, and temporal regions, and decreased ReHo values in the prefrontal and insular regions, and posterior cingulate cortex. Subcortical regions primarily showed decreased ReHo values spanning the caudate, thalamus, globus pallidus, hippocampus, amygdala, parts of the brainstem, and cerebellum. Neurosynth decoding analysis revealed that these patterns of brain activity were related to cognitive processes associated with perception (e.g., attention, spatial attention, visual

980 attention) and least likely with mental suffering and psychological distress (e.g., fear, stress, loss,
981 pain).
982
983
984

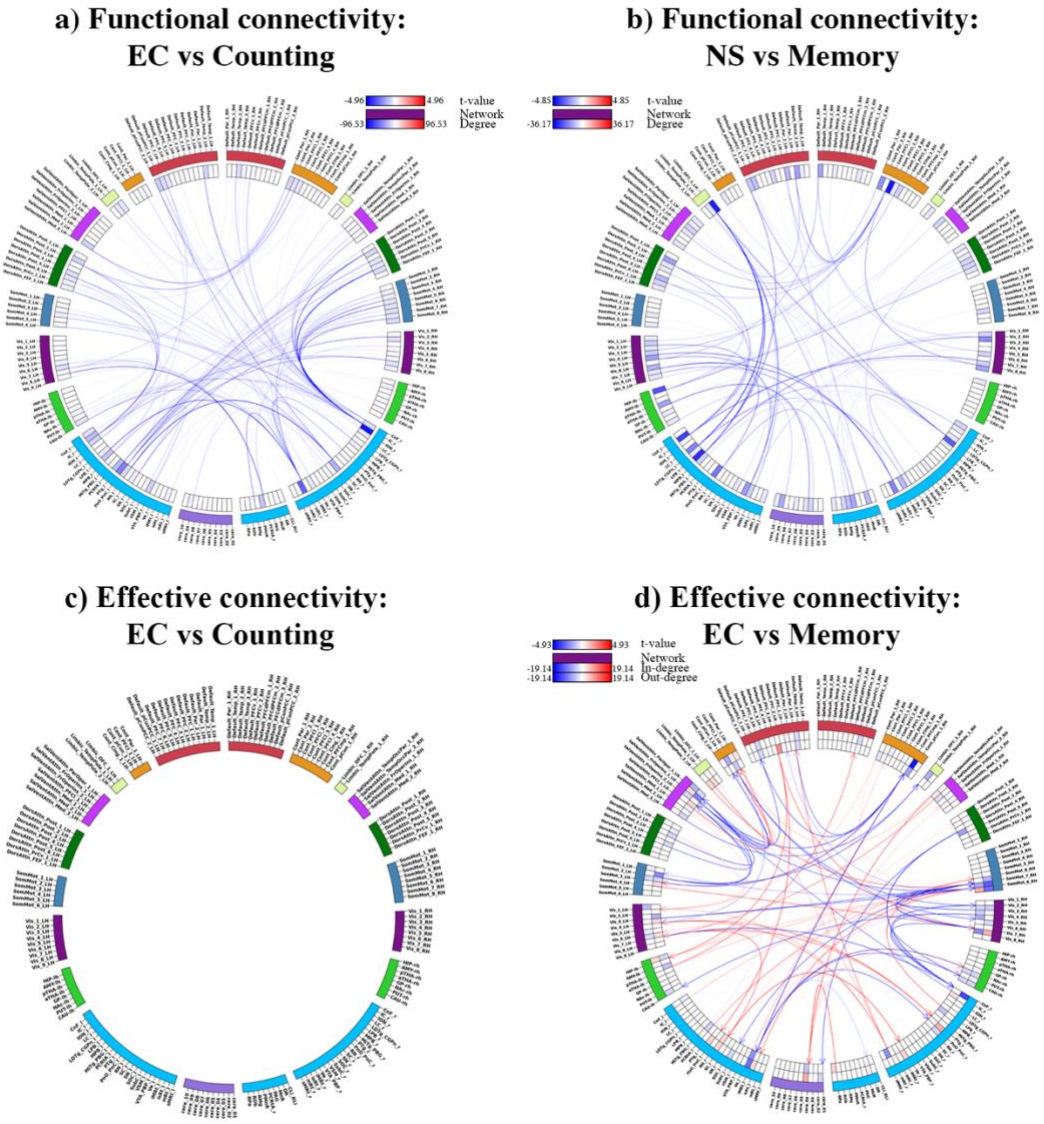

Fig. 3. Differences in functional connectivity and effective connectivity between EC and control conditions. The figure illustrates **(a, b)** functional and **(c, d)** effective connectivity differences between EC and control conditions. Nodes represent brain regions, arranged based on their hemispheric locations and colored according to their network affiliations. For functional connectivity, lines connecting nodes indicate undirected functional connectivity, with blue depicting decreased connectivity. Weighted nodal degrees are represented in the heatmap tracks, depicting the cumulative sum of all its undirected connections. For effective connectivity, directed connections are displayed using arrowheads, with red lines indicating excitatory influence from

995 one region to another in EC relative to controls, and blue lines representing inhibitory influence.
996 Weighted nodal in-degree (incoming connections) and out-degree (outgoing connections) are also
997 illustrated as heat maps.
998

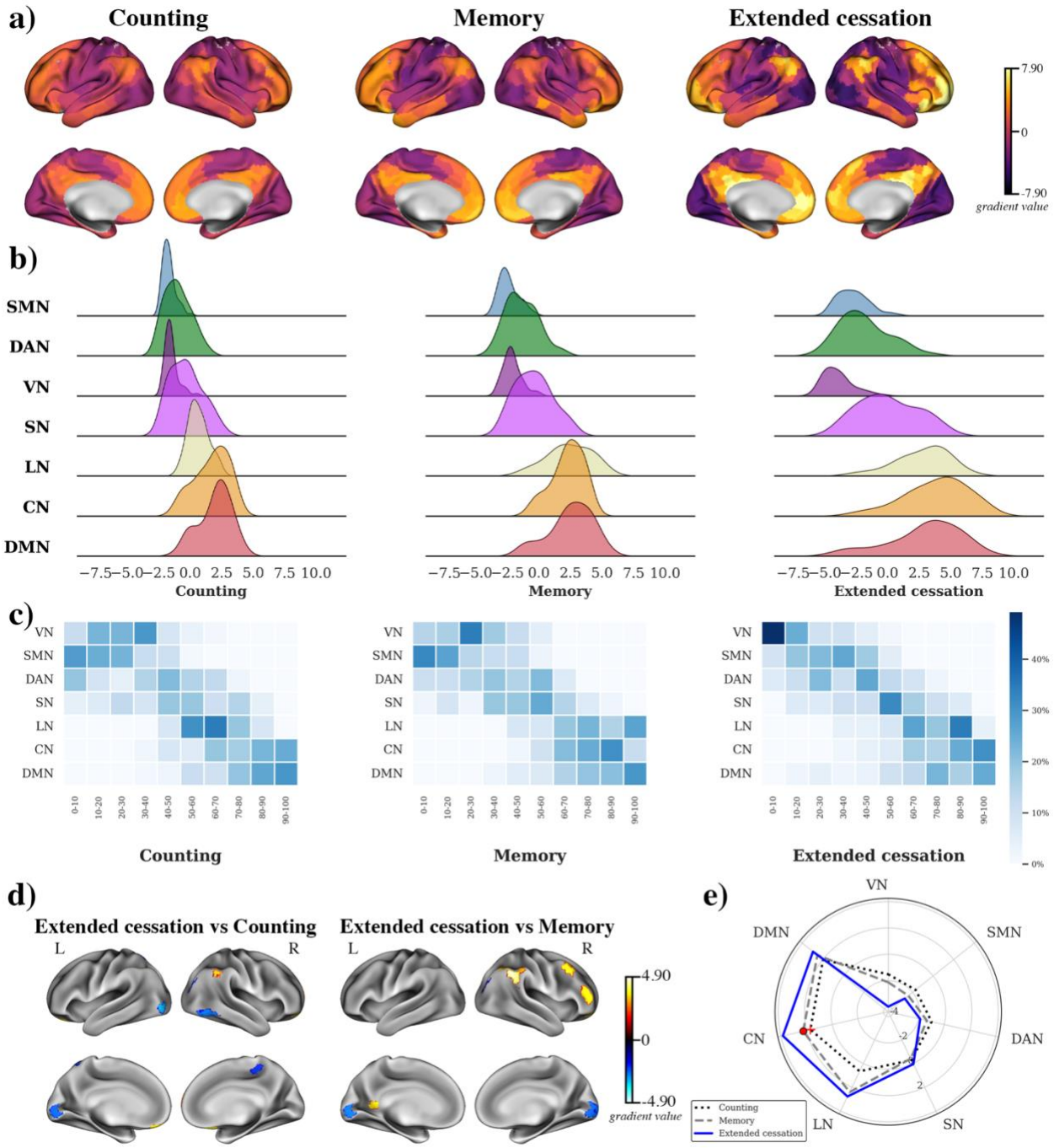

Fig. 4. Differences in principal gradients between EC and control conditions. (a) Average gradients of each condition, demonstrating high gradient values in the transmodal regions during EC compared to control conditions. **(b)** Distribution of gradient values in each network during each condition. Expansion of the gradients were observed across all networks during EC. **(c)** Percentile of gradients along each network during each condition. Gradient values in the lowest 30 percentile during EC were distributed among unimodal regions (VN, SMN, DAN) while

gradient values in the highest 30 percentile during EC were distributed among the LN, CN, and DMN. **(d)** Linear mixed models demonstrated that EC predominantly increases gradient values in the right parietal, and lower gradient values in the left visual cortex. **(e)** Linear mixed models demonstrated that EC exhibited higher gradient values in the CN. The red circle on the plot indicates significance between EC and the control condition. VN = visual network, SMN = somatomotor network, DAN = dorsal attention network, SN = salience network, LN = limbic network, CN = control network, DMN = default mode network.

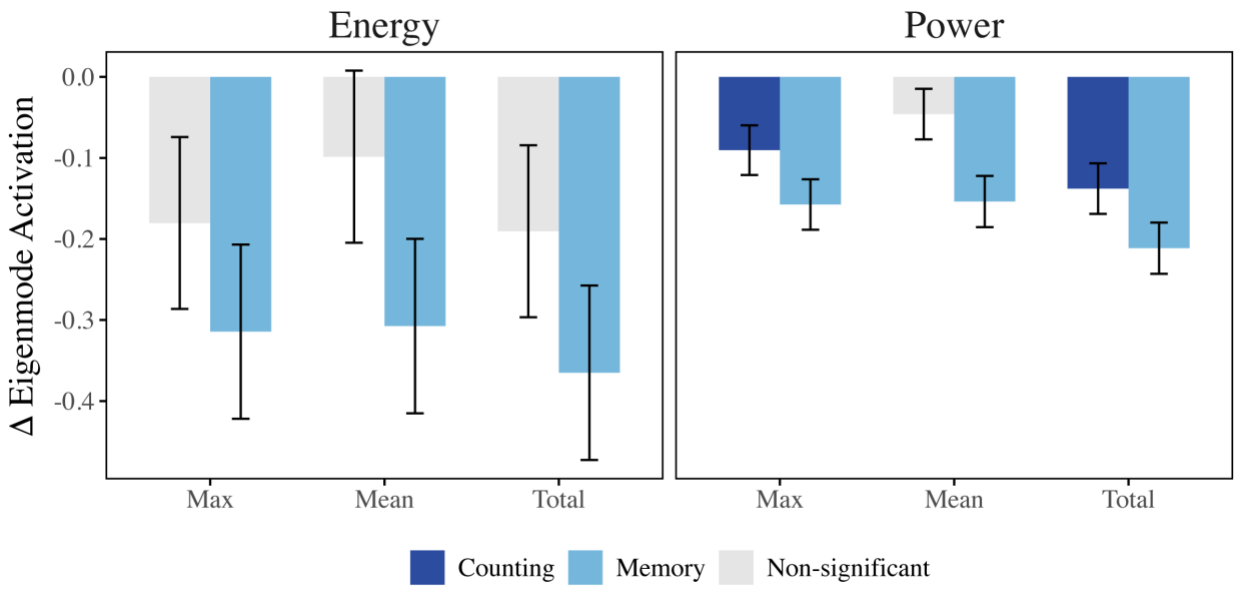

Fig. 5. Differences in global eigenmode activations between EC and control conditions. Difference in global eigenmode activation for mean and max energy and power (averaged across eigenmodes), and total energy and power between EC - counting (dark blue) and EC - memory (cyan) conditions. Non-significant contrasts are colored grey. Error bars signify standard error.

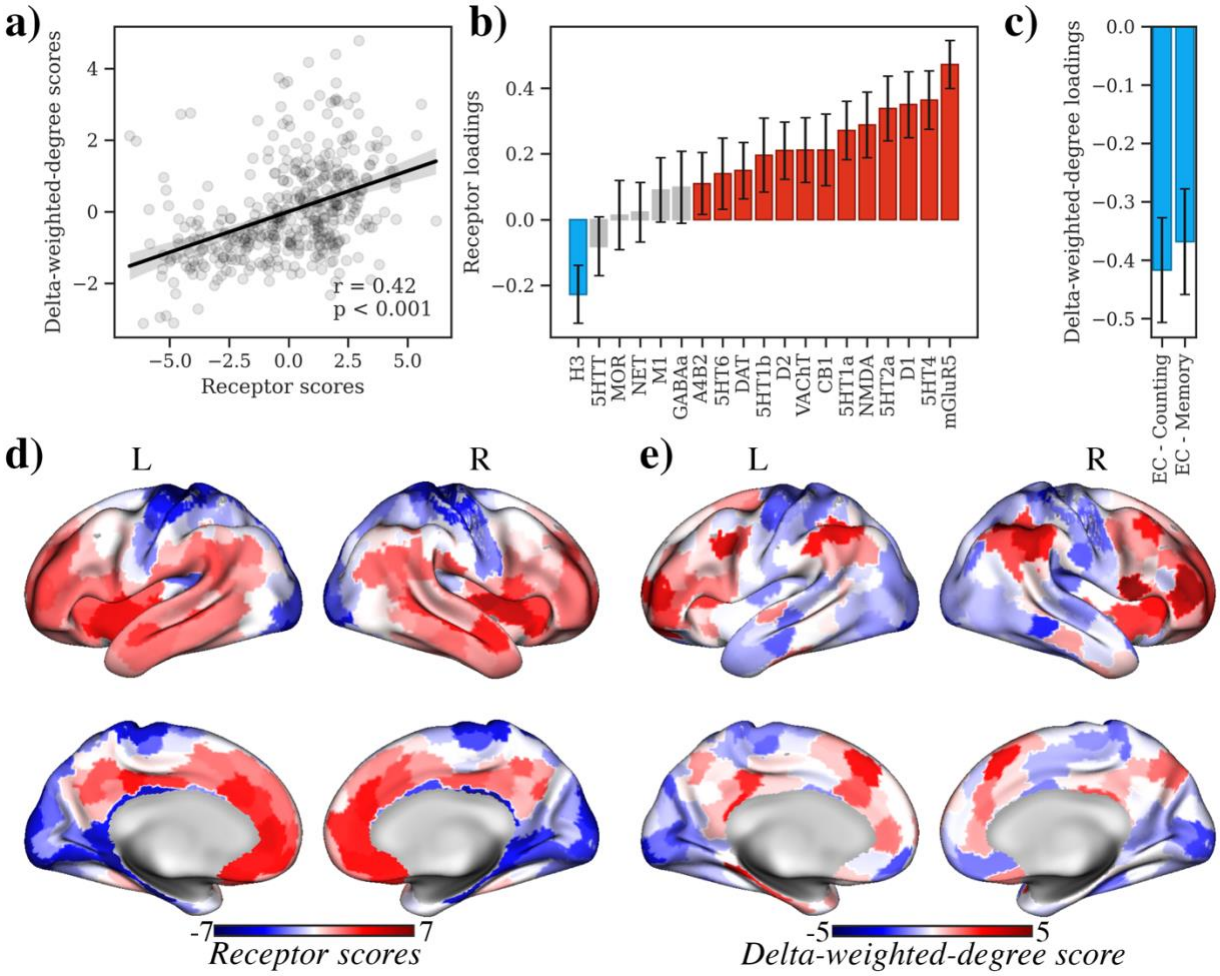

Fig. 6. Spatial relationship between brain activity during EC and neurotransmitter receptor density. Only partial least squares (PLS) component 1 was significant. **(a)** Scatter plot shows the positive correlation between the latent receptor scores and latent delta-weighted-degree scores ($r = 0.42$, $p < 0.001$). **(b)** The bar chart displays the loadings of different neurotransmitter receptors on PLS component 1, with H_3 receptors showing negative loadings while $mGluR_5$, 5HT4, D1, $5HT_{2A}$, and NMDA showing positive loadings. **(c)** The bar chart shows the loadings of delta-weighted-degree maps between task conditions, with negative loadings on the difference between EC and counting (EC - counting) and memory (EC - memory). **(d)** Spatial distribution of coactivation between receptors ('receptor scores') and (**e**) delta-weighted-degree ('delta-weighted-degree scores'). Red areas indicate regions with positive delta-weighted-degree scores, while blue areas represent regions with negative delta-weighted-degree scores.